NJC

New Journal of Chemistry

A journal for new directions in chemistry

Accepted Manuscript

This article can be cited before page numbers have been issued, to do this please use: V. Kumar, S. Kaushal and Y. Singh, *New J. Chem.*, 2025, DOI: 10.1039/D5NJ02044A.

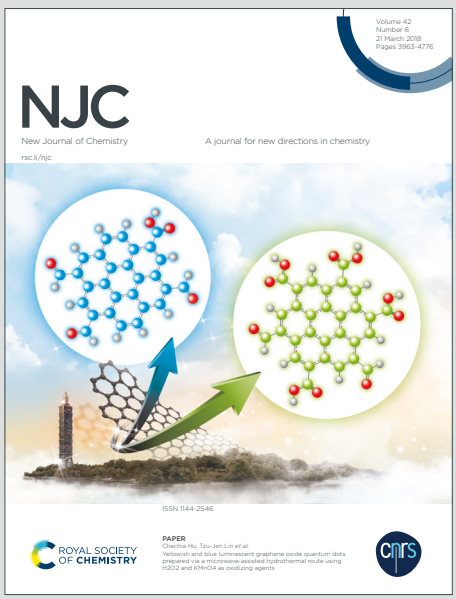

ROYAL SOCIETY OF CHEMISTRY

rsc.li/njc

Biogenic Synthesis of Zinc Oxide Nanoparticles Using Cell-Free Extract of *Spirogyra crassa* (Kütz.) Kütz for Sustainable Biomedical and Environmental Applications

Vinay Kumar[1], Sandeep Kaushal[2*], Yadvinder Singh[3*]

[1]Department of Botany and Environmental Science, Sri Guru Granth Sahib World University, Fatehgarh Sahib, Punjab, India

[2] Regional Institute of Education, NCERT, Ajmer, Rajasthan, India

[3] Department of Botany, Central University of Punjab, Bathinda-151401, Punjab, India

Email of corresponding authors: kaushalsandeep33@gmail.com; yadbotany@gmail.com

Abstract

This study focuses on the biosynthesis of zinc oxide nanoparticles (ZnO NPs) utilizing the cell-free extract derived from the green alga *Spirogyra crassa* (Kütz.) Kütz. A suite of advanced analytical techniques, including FTIR, XRD, FESEM, EDS, HRTEM, XPS, and BET, was employed to confirm the formation and extensively characterize the biosynthesized ZnO nanoparticles. XRD analysis confirmed the formation of a highly crystalline nanomaterial with an average crystallite size of approximately 29 nm. FESEM and HRTEM analyses revealed that the biogenically synthesized ZnO nanoparticles predominantly exhibited a spherical morphology. The biogenically synthesized ZnO nanoparticles exhibit a well-defined crystalline structure, belonging to the hexagonal wurtzite phase with space group $P6_3mc$ (space group number 186). BET analysis revealed that the biogenically synthesized ZnO nanoparticles have a total surface area of 14.97 m^2/g, a pore volume of 0.0342 cm^3/g, and an average pore size of 3.07 nm. The ZnO NPs proved to exhibit significant antidiabetic potential as the sample showed the highest percentage (74.25 % ± 2.7) of enzyme inhibition at 30 µg/ml concentration and IC50 value of α-amylase exhibited at 18.69 µg/ml and for α-glucosidase at 19.06 µg/mL, while in the antioxidant test, 85.15 % ± 3.2 was the highest percentage of 2,2-diphenyl-1-picrylhydrazyl hydrate (DPPH) scavenging activity with IC50 value of 17.90 µg/ml. In addition, the photocatalytic degradation of malachite green dye under sunlight irradiation demonstrated the environmental applicability of the synthesized nanoparticles, achieving a degradation efficiency of 95.7% within 150 minutes. These findings underscore the synergistic biomedical and environmental potential of algal-derived ZnO-NPs for sustainable nanotechnology applications.

Keywords: Biogenic synthesis; Zinc oxide nanoparticles (ZnO NPs); Cell-free extract; *Spirogyra crassa*; environmental remediation

1. Introduction

The mounting existence of perilous organic pollutants and pathogenic bacteria in aquatic environments presents a severe risk to equally ecosystems and human well-being [1]. Wastewater frequently harbors harmful microbes that can cause severe infections, making their exclusion crucial for public safety [2]. Among the various pollutants, synthetic dyes are particularly concerning due to their extensive use across industries such as textiles, pharmaceuticals, and aquaculture [3].

Nanoparticles have a larger surface area than other nano or bulk materials. Moreover, they have distinct physicochemical characteristics owing to their significance in terms of tiny size, surface, and interface. The production of nanoparticles using chemical, physical, and green synthesis methods has been of much interest in recent years [4]. Green synthesis methods are increasingly adopted in materials science due to their potential to facilitate nanoparticle formation through environmentally benign pathways. Such techniques emphasize the reduction of hazardous effluents while ensuring reproducibility, stability, and ecological compatibility [5].

Specifically, green-synthesized nanomaterials derived from algal sources have demonstrated potential in diverse applications such as bioremediation, degradation of synthetic dyes, adsorption of toxic metals, water treatment, agriculture, and food technology. Furthermore, these nanoparticles exhibit promising bioactivities including antioxidant, antibacterial, antifungal, and anticancer properties [6].

Notably, the textile industry alone contributes to approximately 54% of global water pollution, followed by the paint and paper industries, which account for 10% and 8%, respectively. Many dyes utilized in textile manufacturing are known to possess mutagenic and carcinogenic characteristics, thereby representing substantial ecological and health hazards [7]. The most difficult challenges in dye removal from industrial and textile sector effluents are the complicated chemical structure and high resilience of synthetic dyes, which make them resistant to standard treatment procedures [8]. In addition, the introduction of dyes into aquatic systems can lead to pH fluctuations, negatively impacting enzymatic and metabolic functions in aquatic organisms and contributing to biomagnification across trophic levels [9, 10]. Owing to their non-biodegradable nature, these synthetic compounds are resistant to conventional

View Article Online
DOI: 10.1039/D5NJ02044A

wastewater treatment processes and persist in the environment [11]. The textile sector commonly employs several dye classes, including cationic, anionic, and direct dyes, as well as reactive, sulphur-based, indigo, and phthalocyanine variants. Among these, cationic dyes are particularly concerning due to their chemical stability and strong binding affinity, which correlate with elevated toxicity levels arising from their cyclic molecular structures [12].

Malachite green (MG), a synthetic dye of the triphenylmethane group, is widely used in a variety of industries; however, it is known to be very hazardous [13, 14]. Prolonged or high-level exposure to MG has been linked to a variety of adverse health outcomes, such as dermatological reactions like erythema and pruritus, as well as systemic symptoms like cephalalgia, gastrointestinal distress, febrile responses, anaemia, and urine staining [15]. Considering its enduring nature and toxicity, there is a critical requirement for innovative water treatment technologies that are not only effective and inexpensive but also ecologically friendly to provide a safe and sustainable supply of clean water.

To make certain that harmful pollutants are removed efficiently from water systems, ecologically sustainable treatment methods must be used. In the processing of wastewater, a variety of physical, chemical, and biological treatments have been successfully implemented, including sedimentation, flocculation, reverse osmosis, plasma ozonation, membrane filtering, and chemical oxidation [16, 17, 18]. Still, these traditional techniques frequently result in inadequate pollutant removal, principally because they transfer pollutants from one phase to a different one without full mineralization. Photocatalysis is a potential approach for eliminating organic contaminants in water. Solar energy drives redox processes, converting pollutants into less hazardous compounds [19, 20].

Zinc oxide (ZnO), a biocompatible metal oxide semiconductor, is particularly advantageous for intracellular drug delivery applications. It exists in three polymorphic forms: zinc blende, rock salt, and the thermodynamically stable wurtzite phase under ambient conditions, attributed to its tetrahedral coordination between Zn and O atoms. The semiconductor's direct wide band gap (3.1-3.3 eV) supports its versatile functionality in biomedical fields, including antimicrobial systems, targeted drug delivery, biosensing platforms, cosmetic formulations, and therapeutic agents [21, 22]. Because of their tiny size and bio-functionalization, biogenic ZnO nanoparticles are economical, environmentally benign, and exhibit strong photocatalytic activity. Nevertheless, they encounter difficulties such as uneven characteristics and restricted authority over morphology and crystallinity.

Zinc oxide nanoparticles (ZnO NPs) synthesized through biogenic routes are emerging as versatile players in the biomedical arena, offering a sustainable and biocompatible alternative to traditional methods [23, 24]. Beyond their established antibacterial and anticancer properties, these biogenic nanoparticles exhibit significant potential in addressing oxidative stress and managing diabetes. Antioxidant activity is often evaluated using assays like DPPH radical scavenging, where algae-synthesized ZnO NPs demonstrate a significant ability to neutralize free radicals in a dose-dependent manner. These assays quantify the reduction of the DPPH radical by the nanoparticles, indicating their capacity to combat oxidative stress at a cellular level [25]. Furthermore, in vitro antidiabetic potential is assessed through enzyme inhibition assays, such as α-amylase and α-glucosidase inhibition assays. Studies show that biogenic ZnO NPs can effectively inhibit these key enzymes involved in carbohydrate digestion, thereby potentially reducing postprandial glucose levels [26, 27]. These combined therapeutic actions, alongside their utility in drug delivery and wound healing, underscore the broad applicability of ZnO NPs derived through a biogenic route in tackling diverse health challenges. Continued research promises to further unlock their full translational potential in the biomedical field.

Scientists are increasingly using eco-friendly methods to synthesize NPs owing to their low cost, ability to be synthesized in ambient conditions, non-toxicity, environmental compatibility, and ease of execution. The synthesized particles are exceptionally soluble in water, biodegradable, and free of hazardous stabilizers. Various researchers have used a variety of species, including plants, fungi, algae, and bacteria, to synthesize metal/metal oxide NPs [28, 29, 30]. Organismal metabolic byproducts function as lowering and capping agents to enhance stability and biocompatibility. Algae, whether used in dried or live form, have attracted considerable attention as effective "bio-nano-factories" due to their rapid growth and remarkable ability to detoxify harmful metals by converting them into less toxic forms. Their high biomass yield, cultivation without the need for chemicals or fertilizers, and the possibility of multiple harvests per year make them highly appealing for sustainable nanomaterial production [31, 32, 33]. The cell-free extract of green macroalgae is rich in various biomolecules, such as polysaccharides, amides, proteins, amines, pigments, terpenoids, alkaloids, and phenolic compounds that play crucial roles in the reduction and stabilization of metal and metal oxide nanoparticles [34, 35, 36].

The present study reports a green and efficient biosynthetic approach for the fabrication of zinc oxide nanoparticles (ZnO NPs) utilizing a cell-free extract derived from *Spirogyra crassa*

(Kutz) Kütz. *Spirogyra* is a green filamentous algae belonging to the family Zygnemataceae with 400 species reported worldwide. It is one of the most common organisms found in freshwater with a rich phytochemical profile comparable to different medicinal plants [37]. Even though a study on ZnO NPs derived from S. hyalina has confirmed significant bioactivity, including antibacterial and antioxidant properties [38], *S. crassa* is still completely unexplored for NP production. As far as we are aware, this is the first work to use *S. crassa* cell-free extract exclusively for the biogenic production of ZnO NPs. The resulting nanoparticles were comprehensively characterized using a suite of advanced analytical techniques, including Fourier-transform infrared spectroscopy (FTIR), X-ray diffraction (XRD), field emission scanning electron microscopy (FESEM), energy-dispersive X-ray spectroscopy (EDX), high-resolution transmission electron microscopy (HRTEM), Brunauer–Emmett–Teller (BET) surface area analysis, and X-ray photoelectron spectroscopy (XPS), to evaluate their structural, morphological, and surface properties. Furthermore, GC-MS profiling of the algal extract was performed to correlate specific phytochemicals with the observed functional properties, adding mechanistic insight to the green synthesis approach. With their unique morphologies and surface functionalization, the biosynthesized ZnO NPs produced in this work show promise for both the photocatalytic degradation of malachite green dye and in vitro biomedical applications. This innovative technique broadens the scope of sustainable nanoparticle manufacturing techniques and shows promise for complementary uses in the environmental and medicinal domains.

2. Materials and methods

2.1 Chemicals

In this study, all chemicals of analytical-grade quality were utilized. To maintain consistency and prevent contamination, double-distilled water was used. Zinc nitrate hexahydrate ($Zn(NO_3)_2 \cdot 6H_2O$ ≥98% purity, AR grade) of Loba Chemie Pvt. Ltd, served as the zinc precursor. Sodium hydroxide pellets (NaOH pellets, ≥98% purity, analytical grade), procured from Sigma-Aldrich, were used to adjust the reaction conditions. Ethanol (≥99.9% purity, analytical grade) was used as a washing solvent to eliminate organic residues. DPPH (1,1-diphenyl-2-picrylhydrazyl, ascorbic acid (≥99%, AR grade), α-amylase, acarbose, phosphate buffer, α-glucosidase enzyme, potassium sodium tartrate tetrahydrate, para-nitrophenyl-α-glucopyranoside, starch, hydrochloric acid (HCl) and DMSO from HiMedia Laboratories were used for antioxidant and antidiabetic assays. Malachite green (MG, chemical formula:

$C_{23}H_{25}ClN_2$, molecular weight: 364.91 g mol^{-1}, dye content ≥90%) of HiMedia Laboratories, India, was selected as the model pollutant for the photocatalytic degradation experiments.

2.2 Collection of Algal Biomass

The algal biomass was collected from the pond located at Fatehgarh Sahib and brought to the laboratory for further processing. The biomass was cleaned with DD H_2O and observed under a light microscope and identified as *Spirogyra crassa* (Kütz.) Kütz. The important characteristics of these algae are, it is an unbranched filamentous chain of cylindrical cells with have size width from 40–92µm and in length from 80–223 µm. In this species, there is a presence of bilayer cell wall, nucleus, pyrenoid, and spiral-shaped chloroplasts within each cell appeared as a "spring-like" structure. After the identification of the biomass was kept at 25℃ (room temperature) for dry [39].

2.3 Gas chromatography-mass spectroscopic analysis of *S. crassa* extract

The GC–MS–based identification and quantification of biomolecules present in the methanolic extract of the organism was carried out by using a Shimadzu QP 2010 Ultra system (Shimadzu, Tokyo, Japan). The extract was processed by the earlier described methodologies, incorporating slight methodological refinements to enhance detection accuracy [40]. The prepared cell extract was filtered through a 0.22 µm syringe filter to remove particulates, and 1 µL aliquot of each filtered solution was loaded onto GC vials and injected onto the GC-MS system. The separation was achieved using a capillary column with Helium (99.99 % purity) as the carrier gas at a constant flow rate of 1.60 mL/min. The initial oven temperature was set at 60 °C (held for 0.2 min), and it was ramped to 180 °C at 20 °C/min (held for 3 min) and subsequently to 280 °C at 15 °C/min (held for 3 min). The analysis was done in EI mode with mass range scanned from m/z 35 to 800 for a total run time of 18.87 minutes. The compound identification was carried out by comparing the mass spectra with entries in the NIST20 mass spectral library.

2.4 Preparation cell-free extract of algae

To prepare the extract, 10 grams of dried algal biomass was crushed into fine powder with a pestle and mortar. Mixed the crushed fine powder with 100 ml DD H_2O in a 250 ml glass beaker and heated it for one hour at 70 to 80 °C with periodical stirring. After one hour, allow the mixture to cool at room temperature and centrifuge at 5000 rpm for 12 minutes to get the extract and then the extract was filter into Erlenmeyer flask with Whatman No. 1 filter paper and kept in a refrigerator at 4°C for later use in nanoparticle synthesis.

View Article Online
DOI: 10.1039/D5NJ02044A

2.5 Synthesis of ZnO NPs

An aqueous solution 0.5 M zinc nitrate hexahydrate was prepared in a 250 mL beaker. The 10 mL cell-free extract of *S. crassa* was added dropwise into the 0.5 M 90 mL solution of Zn $(NO_3)_2.6H_2O$ (zinc nitrate hexahydrate). The mixture solution was maintained at 60 to 80 °C on a magnetic stirrer for one hour. The pH of the reaction mixture was adjusted between 7 to 8 by using sodium hydroxide. The cell-free extract facilitated the reduction of zinc ions (Zn^{2+}) to form zinc oxide (ZnO). The appearance of a light-yellow colour confirms the fabrication of ZnO NPs. The reaction mixture was placed in the dark for complete bio-reduction, and saturation and centrifugation were done for 12 minutes at 12000 rpm. After centrifugation, the pellet was centrifuged, the obtained pellet was washed twice with DD H_2O to remove other contaminants. Synthesised ZnO NPs were dried in an oven and kept at 4 °C in a refrigerator for further use. The synthesis of ZnO nanoparticles was confirmed by using different spectrophotometric analyses [41].

2.6 Characterization of ZnO nanoparticles

The bio-reduction of ZnO NPs from zinc ions was analysed by using FTIR (Parkin Spectrum-400) to analyse the occurrence of functional groups accountable for the ZnO nanoparticles synthesis. The frequency range of light absorption was measured at a wave number range of 4000-400 cm^{-1}. The size, shape, and crystalline nature of ZnO NPs in the 2θ ranges of 0 to 100 degrees were analysed by using XRD spectroscopy (PANalytical X`Pert Pro). To examine the morphology (e.g., particle shapes and sizes) of ZnO NPs that interact with particles with negative charge (electrons) was analysed by using FESEM (Carl Zeiss supra-55). The presence and concentration of elements in the sample in the range of 0-20 keV were analysed by using EDX spectroscopy (Carl Zeiss supra-55). Morphology of nanoparticle studied by using HRTEM (JEOL JEM 2100 Plus), the high magnifications used are enough to simply get the lattice spacing of inorganic materials, and also performed SAED pattern to evaluate crystallinity and positions of nanoparticles. BET (Quantachrome TouchWin™ v1.22) was used to examine the pore width, pore volume, and surface area of the nanoparticle through gas adsorption analysis. XPS (Thermo Fischer Scientific ESCALAB Xi+) was studied to understand the presence of chemical state and composition of the elements in ZnO NPs using characteristic energy 1486.6 eV.

2.7 Biomedical applications of biogenic ZnO NPs

2.7.1 Antioxidant activity

The antioxidant capacity of zinc oxide nanoparticles (ZnO NPs) was evaluated using the 1,1-diphenyl-2-picrylhydrazyl (DPPH) assay. For the experiment, a 0.14 mM DPPH solution was prepared in methanol and kept in the dark at room temperature. The separate standard solutions of ascorbic acid and ZnO NPs, ranging in concentration from 2.5 to 30 µg/mL, were made using a 1:1 mixture of methanol and ethanol. Subsequently, varying concentrations of the ZnO NPs solution (860 µL) were mixed with 140 µL of the DPPH solution and incubated in the dark at 50°C for 30 minutes. A DPPH solution without nanoparticles served as the negative control, and ascorbic acid was used as the positive control. The absorbance of each mixture was measured at 517 nm using a UV–Vis spectrophotometer [42, 43]. The percentage of DPPH radical scavenging activity by the ZnO NPs was then calculated using a specific formula (equation 1).

$$\%\ Inhibition = \frac{[A_0 - A_1]}{A_0} \times 100 \qquad \ldots 1$$

Where: A_0 = Absorbance of the control, A_1 = Absorbance of the sample

2.7.2 Antidiabetic assay

2.7.2.1 α-amylase

The synthesized ZnO-NPs were evaluated for their antidiabetic properties by examining their inhibitory effect on α-amylase activity. The assay was performed based on established methods with certain modifications [44]. The reaction mixture consisted of 15 µL phosphate buffer, 25 µL α-amylase solution, 10 µL of the ZnO-NPs at various concentrations, and 40 µL starch substrate. This mixture underwent incubation at 50 °C for 30 minutes. Subsequently, the reaction was terminated by adding 20 µL of HCl solution, followed by the addition of 90 µL of iodine solution for colour development. For control purposes, DMSO was used as a negative control, and acarbose (µg/mL) served as a positive control. A blank sample containing only starch and buffer was also included. The absorbance of the final solutions was measured at 540 nm to quantify the extent of enzyme inhibition, which was determined using a specific calculation [45, 46]. The percentage inhibition of α-amylase activity was calculated using equation 2:

$$\%\ Inhibition = \frac{[A_0 - A_1]}{A_0} \times 100 \qquad \ldots. 2$$

Where: A_0 = Absorbance of the control, A_1 = Absorbance of the sample

2.7.2.2 α-glucosidase

View Article Online
DOI: 10.1039/D5NJ02044A

Synthesized ZnO nanoparticles at various concentrations (20–150 µg/mL) were suspended in 0.2 M Tris buffer (pH 8.0) and incubated with 2% (w/v) maltose or sucrose for 5 minutes at 37 °C. Afterward, 1 mL of α-glucosidase enzyme (1 U/mL) was added, followed by incubation at 35 °C for 40 minutes. The reaction was halted using 2 mL of 6 N HCl. Acarbose (µg/mL) was employed as a positive control. Absorbance was recorded at 540 nm [47]. α-glucosidase inhibition was calculated using equation 3:

$$\%\ Inhibition = \frac{[A_0 - A_1]}{A_0} \times 100 \qquad \ldots. 3$$

Where: A_0 = Absorbance of the control, A_1 = Absorbance of the sample

2.8 Environment Applications

2.8.1 Dye degradation studies

The potential of biogenic fabricated ZnO NP for photocatalysis was evaluated based on the extent to which they degraded MG dye. Probe molecules, specifically malachite green (Mw = 365.9, λ_{max} = 617 nm), were employed to examine the breakdown of these compounds in synthetic wastewater when biogenic fabricated ZnO NPs were introduced. The 200 mg as-prepared biogenic synthesized ZnO NPs were examined by dispersing them in 50 mL of wastewater contaminated with synthetic dyes at a concentration of 10 ppm. To achieve the adsorption equilibrium between the nanoparticles and dye, the solution was acclimatized for 60 minutes in the dark while being constantly stirred. The dye solution that had been equilibrated with NPs was then subjected to direct sunlight to examine the biogenic ZnO NPs' photocatalytic activity for dye degradation. To keep the NPs' consistent catalytic activity during the bulk phase, the system was constantly shaken. At different intervals of 5, 10, 15, 20, 25, and 30 minutes, the degraded dye samples were assembled to assess the degree of dye decolorization in the samples. The specimens collected were separated from the NPs by centrifuging them at 10,000 rpm, and the supernatant was then used to assess absorbance before any spectroscopic observations were made. Equation 4, was used to calculate the ZnO NPs' time-based photocatalytic dye degradation efficiency (η):

$$\eta = (\frac{A_0 - A_t}{A_0}) \times 100 \quad \ldots\ldots..4$$

where the absorbance of the dye sample is A_0 and A_t collected before the start (0 min) and at a given time (t min) of photocatalytic dye degradation.

3. Results and Discussion

View Article Online
DOI: 10.1039/D5NJ02044A

3.1 Phytochemical analysis of *S. crassa* cell free extract

Gas chromatography–mass spectrometry (GC–MS) analysis of the *S. crassa* cell-free extract identified 28 phytochemical constituents, spanning several categories including fatty acid esters, alkanes, phenolic compounds, ketones, siloxanes, saponins, and sterols (Fig. S1, Table S1). Notable components included Phenol, 3,5-bis(1,1-dimethylethyl)-, known for its dual antioxidant and antimicrobial roles; Pseudosarsasapogenin-5,20-dien methyl ether, a steroidal saponin linked with antidiabetic and free radical-scavenging activity; and 11-Octadecynoic acid methyl ester, previously reported for its antimicrobial and anticancer efficacy. Other biologically relevant compounds, such as 9,12-Octadecadienoic acid methyl ester and 25-Hydroxycholesterol dimethyl ether, were associated with anti-inflammatory and immunomodulatory functions. The identification of 3-Isopropoxy-1,1,1,7,7,7-hexamethyl-3,5,5-tris(trimethylsiloxy)tetrasiloxane, a siloxane derivative used in drug delivery systems, points to the biomedical versatility of the extract. The prevalence of alkanes, oxysterols, and fatty acids suggests that the extract serves not only as a bio-reductant and stabilizer in nanoparticle synthesis but also as a contributor to the enhanced bioactivity of the resulting ZnO nanoparticles.

3.2 Characterization of biogenic ZnO NPs

3.2.1 UV spectrophotometric analysis

UV-vis spectroscopy validated the fabrication of ZnO NPs in the 250-800 nm region. The absorption spectra of green produced ZnO NPs revealed a distinct peak at 330 nm (Fig. S2).

3.2.2 FT-IR analysis

The FT-IR analysis of biogenic fabricated ZnO NPs was performed over the infrared range of 500–4000 and the results are displayed in Fig. 1a. The results displayed fundamental mode of vibrations at 3440 cm^{-1}, 1628 cm^{-1}, 1377 cm^{-1},1220 cm^{-1},1120 cm^{-1}, and 560cm^{-1}, respectively. The peak at 3440 cm^{-1} was due to the –OH stretching of phenolic alcohol. The occurrence of -C=O stretching vibration owing to esters and carboxylic acids was shown by the characteristic peak at 1625 cm^{-1}. Following the –OH bending vibration modes of phenolic groups and the –CH_2 stretching vibrations of carbon chains, respectively, peak values at 1380 $cm^{-1}$and 1236 cm^{-1} were detected. The distinctive peak at 1077 cm^{-1} is associated with the stretching vibrations of C–O–C. Finally, the peak at 560 cm^{-1} is due to the existence of Zn-O stretching vibration and confirms the synthesis of ZnO NPs [48]. The *S. crassa* extract's FTIR spectrum reveals peaks at 3300 cm^{-1}, 1630 cm^{-1}, and 1000-1200 cm^{-1} are correspond to O–H stretching

vibrations, C=O stretching of carbonyl groups, and C–O–C or C–O stretching vibrations, respectively (Fig. 1b). These functional groups suggest the presence of biomolecules such as polyphenols, proteins, and carbohydrates, which contribute to nanoparticle formation.

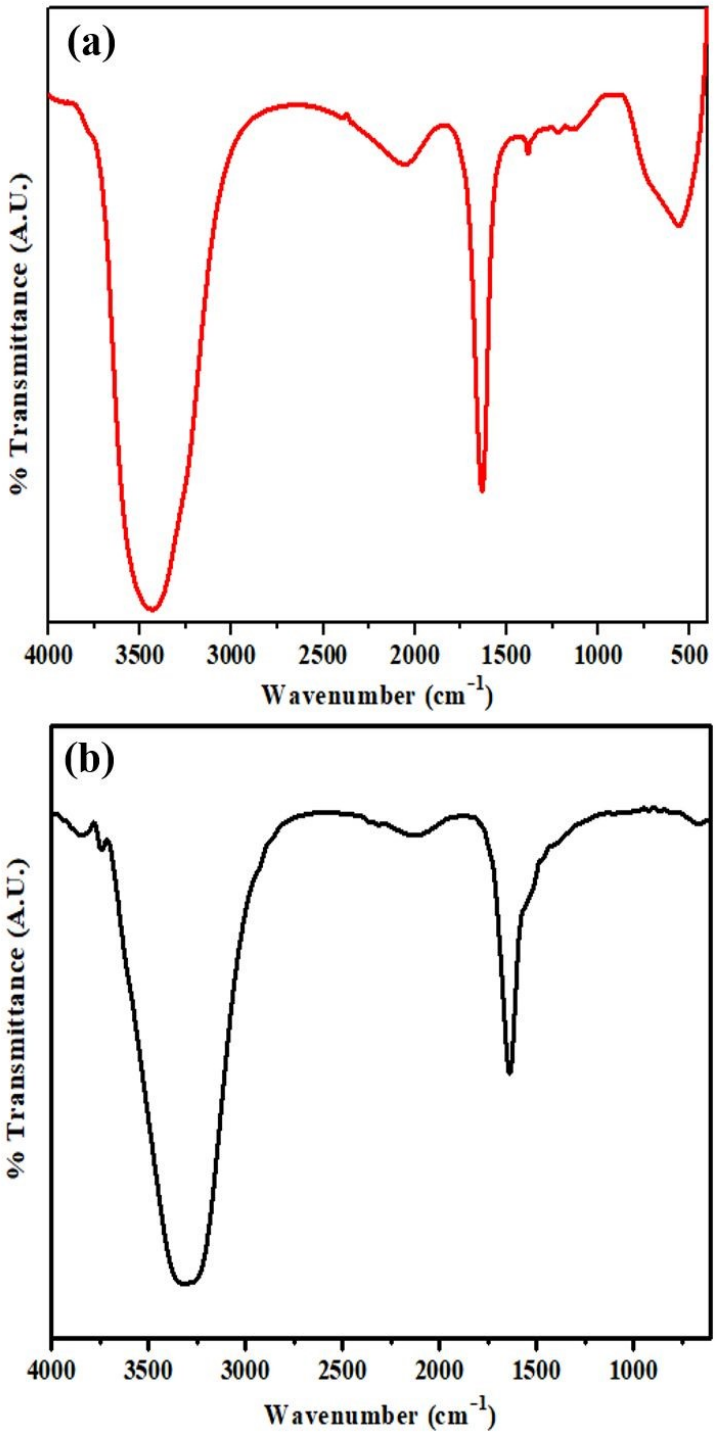

Fig. 1 FTIR spectrum of a) biogenic ZnO NPs and b) *S. crassa* extract

3.2.3 X-ray diffraction studies (XRD)

Furthermore, XRD study was carried out to confirm the phase purity and crystallinity of the biogenic fabricated ZnO NPs (Fig. 2a). The XRD pattern of ZnO nanoparticles is displayed diffraction bands at 31.7° (100), 34.4° (002), 36.3° (101), 47.5° (102), 56.6° (110), 62.8° (103), 66.3° (200), 67.9° (112), 69.1° (201), 72.5° (004) and 76.7° (202) corresponding to hexagonal symmetry in the ZnO NPs crystalline structure. The biogenic synthesized ZnO NPs have a crystalline structure having space group P63mc, with space group number 186, and well matched with the standard JCPDS (03-065-3411). These peaks matched the Joint Committee on Powder Diffraction Standards (JCPDS) card number. 03-065-3411 (Fig. 2(b)), which confirmed the synthesis of phase-pure ZnO without detectable impurities. The crystal size of as-prepared nanoparticles was determined using Scherrer's equation and was found to be ~29 nm.

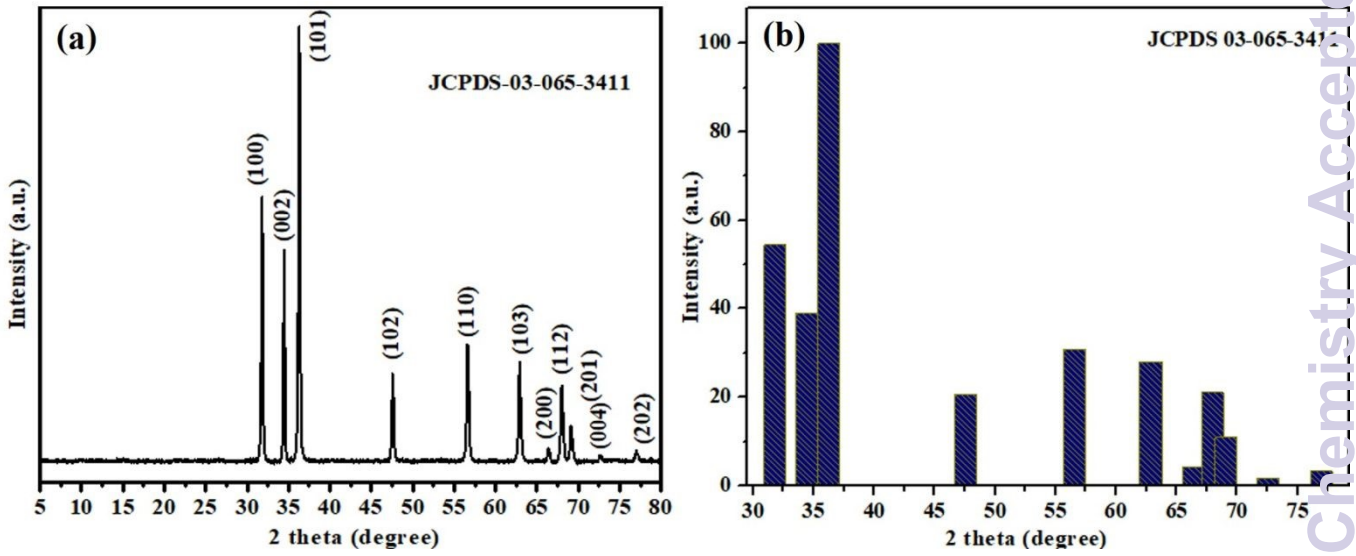

Fig. 2 a) XRD pattern and b) Joint Committee on Powder Diffraction Standards of ZnO NPs

3.2.4 Morphological studies

The structural morphology of the biogenic synthesized ZnO nanoparticles was examined by FESEM and HRTEM (Fig.3). It is discernible from FESEM images that the particles possessed a roughly spherical shape with the particle size distribution of 25–75 nm with clearly defined grain boundaries (Fig. 3a&b). It was discovered that the particles had been uniformly gathered, giving the structure the appearance of a hierarchical sheet. Further, the HRTEM studies were employed to investigate the internal structure of as-prepared ZnO NPs (Fig. 3c-e). Here, we discovered uniformly aggregating spherical ZnO nanoparticles. The lattice fringes observed in Fig. 3f display characteristic features of ZnO nanoparticles, with an interplanar spacing of 0.25 nm, corresponding to the (101) crystallographic plane. The selected area electron diffraction

View Article Online
DOI: 10.1039/D5NJ02044A

(SAED) pattern exhibits distinct and well-defined diffraction rings, indicative of the polycrystalline nature of the synthesized nanoparticles. The corresponding lattice planes are indexed to (100), (002), (101), and (110), as shown in Fig. 3g, which are in excellent agreement with the X-ray diffraction (XRD) analysis, thereby confirming the crystalline structure of the ZnO nanoparticles. Further, Energy-dispersive X-ray spectroscopy (EDS) was employed to analyse the elemental composition of the synthesized ZnO nanoparticles. The structural characteristics of the nanoparticles appear to promote uniform elemental distribution, potentially reducing particle agglomeration. This is corroborated by the elemental mapping images presented in Fig. 3h, which demonstrate a homogeneous dispersion of zinc (Zn) and oxygen (O) across the nanoparticle surface.

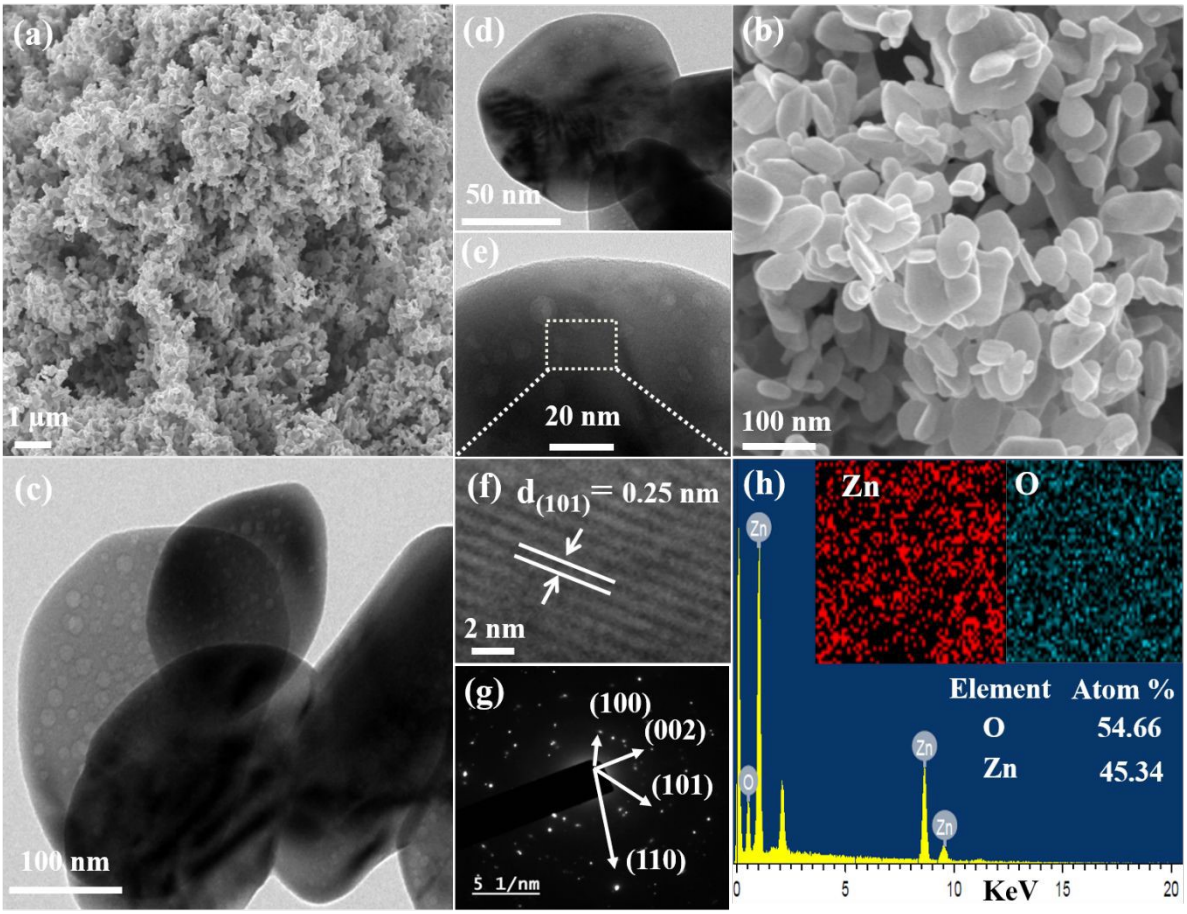

Fig. 3 a-b) FESEM images; c-f) HRTEM images; g) SAED pattern and h) EDS and elemental mapping of ZnO NPs

3.2.5 XPS

XPS is an essential technique in order to obtain an in-depth understanding of the chemical state and composition of as-synthesized nanoparticles (Fig. 4). According to the survey spectrum,

the main elements are Zn, O and C. The Zn 2p spectrum displays two bands at binding energy of 1044.5 eV and 1021.5 eV, respectively for $Zn2p_{3/2}$and $Zn2p_{1/2}$ [49]. Gaussian fitting is applied to deconvolute the O 1 s peak into three peaks at 529.9, 530.5 and 531.7 eV. The oxygen atoms in the oxide lattice with and without oxygen vacancies are designated by the peaks at 529.9 and 530.5 eV, respectively [50]. Whereas, the third peak of O 1s at 531.7 eV is attributed to oxygen of hydroxyl (Zn-OH) group adsorbed on ZnO NPs [51]. The C 1s spectrum can be subdivided into three peaks at 283.7eV, 284.5eV and 285.8 eV corresponding to C-C, C-O and C=C, respectively.

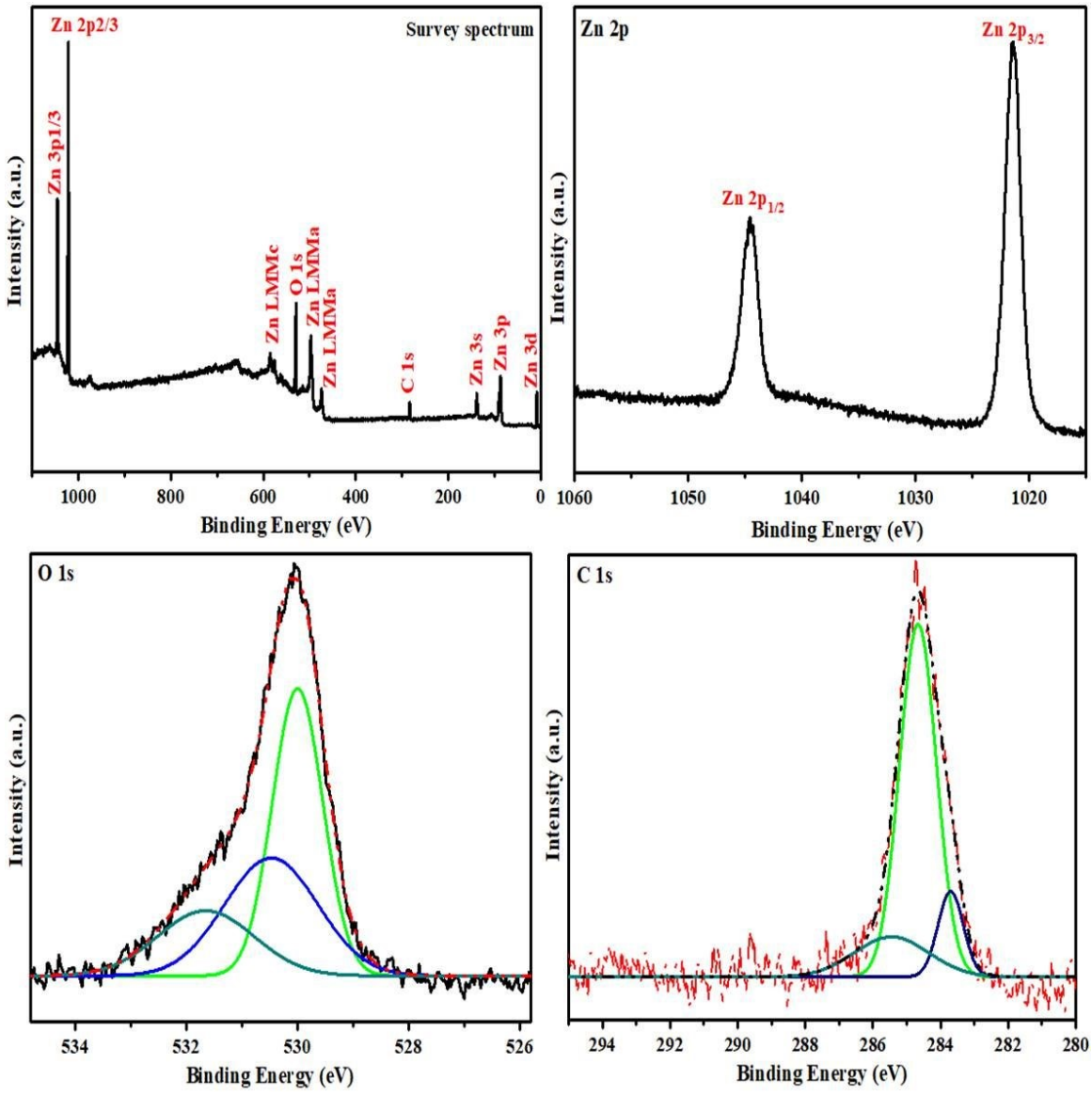

Fig. 6 XPS spectra of ZnO NPs

3.2.6 BET analysis

The BET investigation was used to determine the surface area, pore diameter and pore volume of biogenic synthesized ZnO nanoparticles. Fig. 5 shows the nitrogen adsorption–desorption

isotherm and the Barrett–Joyner–Halenda (BJH) plot. The isotherm of type IV featuring the H3 hysteresis loop observed in the relative pressure range between 0.86–0.97 is demonstrated by the nitrogen adsorption/desorption isotherm. Further, it has been observed from the BET results that total surface area, pore size and pore volume of the biogenic synthesized ZnO nanoparticles have been determined to be 14.97m^2g^{-1}, 0.0341964 cm^3g^{-1} and 3.06764 nm, respectively. As a consequence, the ZnO nanoparticles' small pore structure and remarkably homogeneous outer surface promote surface info. Henceforth, the ZnO nanoparticles have a remarkably homogeneous outer surface and small pore structure that is promising for surface interactions.

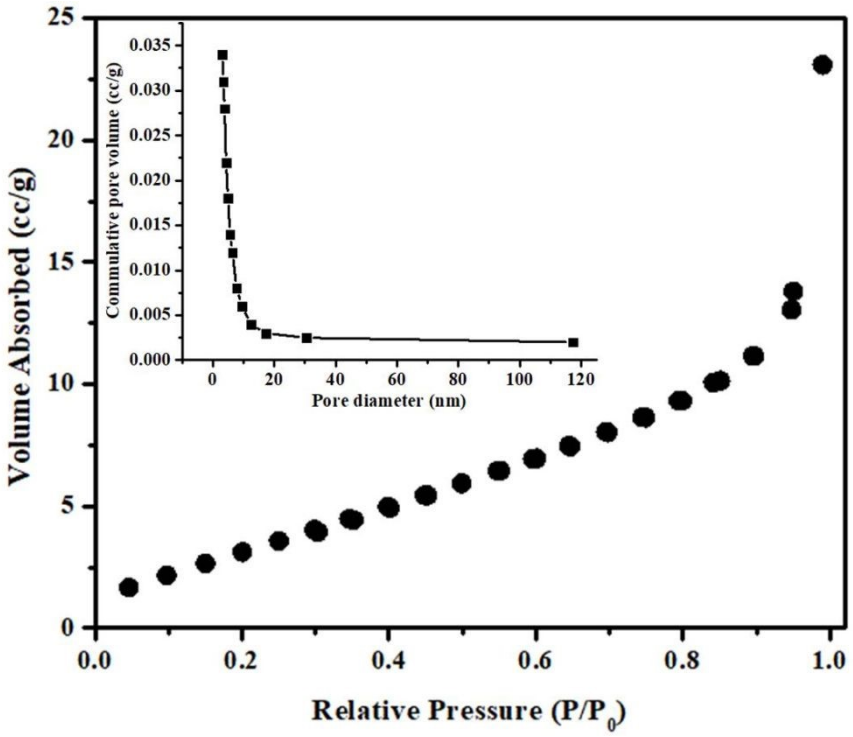

Fig. 5 N_2 adsorption–desorption isotherm (inset BJH plot) of ZnO NPs

3.3 Biomedical application of the biogenic ZnO NPs

3.3.1Antioxidant activity

The antioxidant potential of synthesized biogenic zinc oxide nanoparticles (ZnO NPs) was evaluated using the DPPH assay (Fig. 6). This assay measures the ability of the NPs to neutralize DPPH, a stable free radical, leading to a reduction in its characteristic color. The concentration at which 50% of the DPPH radicals were neutralized (IC50) for synthesized biogenic ZnO NPs was found to be 17.90 µg/ml. In comparison, the IC50 of ascorbic acid, a standard antioxidant, was 14.48 µg/ml. These results indicate that the synthesized biogenic ZnO NPs demonstrated significant free radical scavenging activity that increased with

concentration. Previous research has also explored the antioxidant activity of ZnO NPs synthesized using biological methods, including those mediated by algae. Studies have shown that ZnO NPs derived from algal extracts exhibit significant antioxidant properties. For instance, some research has reported that ZnO NPs synthesized using green algae demonstrate strong DPPH scavenging activity, highlighting the potential of these biogenic nanoparticles in antioxidant applications. The antioxidant activity of algal-mediated ZnO NPs is often attributed to the presence of various bioactive compounds in the algal extracts, which act as reducing and capping agents during nanoparticle synthesis and contribute to the overall antioxidant potential.

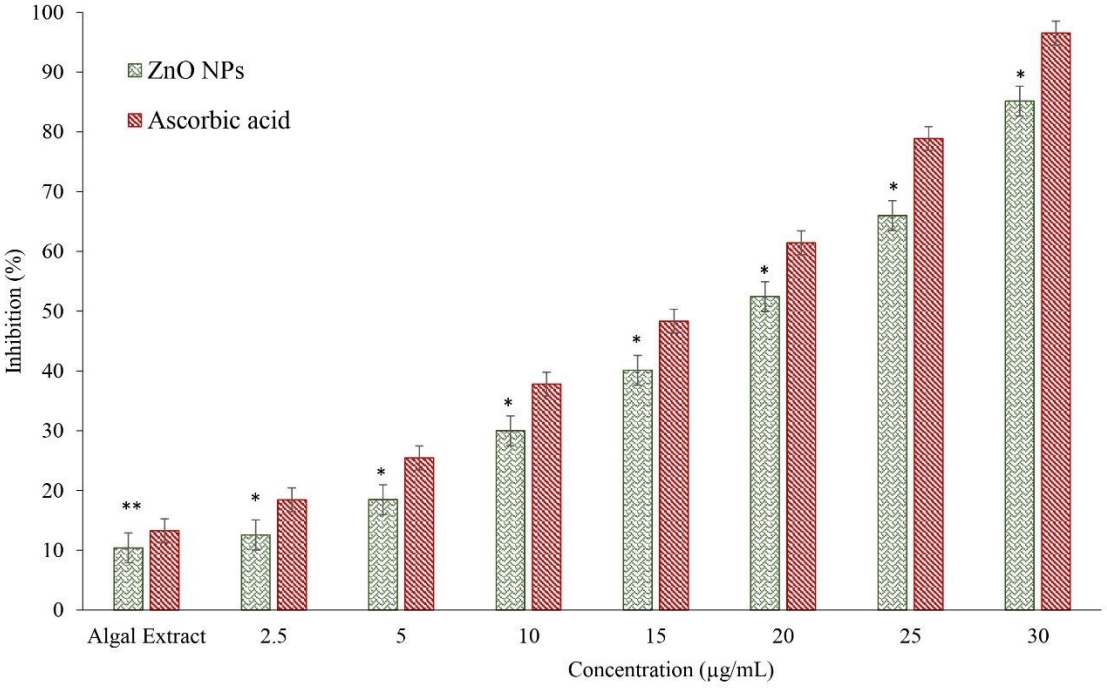

Fig. 6 DPPH scavenging activity of synthesized ZnO nanoparticles. *The value marked with *signify significant at 1% level of significance*

3.3.2 Antidiabetic Assay

The results of our study revealed that biosynthesized zinc oxide nanoparticles (ZnO NPs) significantly inhibit the α-amylase and α-glucosidase activity on concentration dependent manner (Fig. 7). A significant difference in suppression was noted between 2.5 and 30 µg/ml concentration of biosynthesized ZnO NPs. The IC50 value of ZnO NPs calculated for α-amylase was 18.69 µg/ml and for α-glucosidase was 19.06 µg/mL indicating their significant inhibitory potential, while acarbose (positive control) showed an IC50 of 15.02 µg/ml (Fig. 7).

View Article Online
DOI: 10.1039/D5NJ02044A

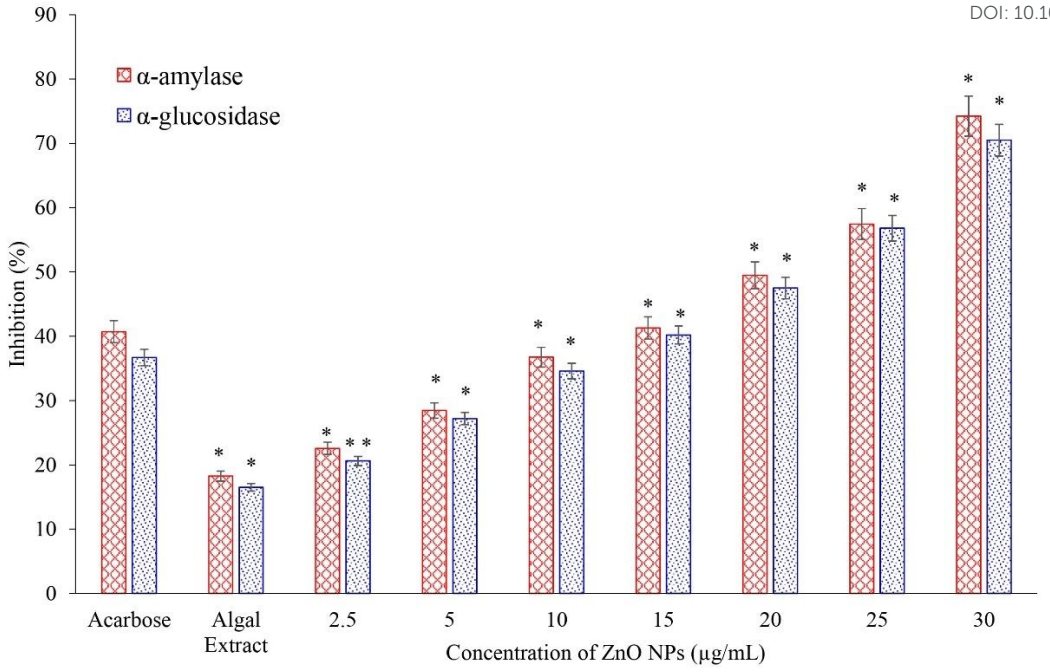

Fig. 7 α-amylase and α-glucosidase inhibition activity of synthesized ZnO nanoparticles. *The value marked with *, ** signify significant at 1% and 5% level of significance*

These findings suggest that biologically synthesized ZnO NPs possess promising antidiabetic properties, offering a potentially effective, affordable, and sustainable approach to diabetes treatment. The previous research on algal-mediated ZnO NPs corroborates the bioactivity of these nanomaterials, demonstrating their synthesis using various algae and their applications, including antidiabetic effects. Algal-derived ZnO NPs often exhibit unique properties influencing their biological activity. While this study highlights α-amylase inhibition, other work has explored their impact on α-glucosidase and their biocompatibility. The IC50 value of 18.69 µg/ml and 19.06 µg/mL for these algal-mediated ZnO NPs is comparable to some reported values, suggesting potential for antidiabetic applications, although slightly less potent than acarbose. Future research could investigate the inhibition mechanisms, in vivo effects and optimize synthesis for enhanced efficacy.

3.3 Photocatalytic efficiency of the biogenic ZnO NPs

Fig.8 displays the results of the photocatalytic activity of MG dye breakdown. It was discovered that the algal extract-based biogenic fabricated ZnO NPs exhibited outstanding photocatalytic efficiency for the dye destruction. The absorbance properties of MG-polluted solution specimens at different stages of the photocatalytic breakdown are shown in Fig.10.

During the initial 60 minutes of the photocatalysis, there was a significant decline in the absorption peak intensity that finally vanished entirely after 150 minutes. The time curve of the deterioration rate of MG dye is shown in Fig. 8. After 60 minutes of photocatalysis, almost 57.6% of the total MG concentration had been broken down, and after 150 minutes, the MG breakdown rate was 95.7%. The kinetics of dye decomposition have been described by a fast early phase and a slow secondary phase. Initially in the process of photocatalysis, the rapid rate of decomposition of dye was facilitated by the abundance of catalytic sites and the wider concentration range [52].

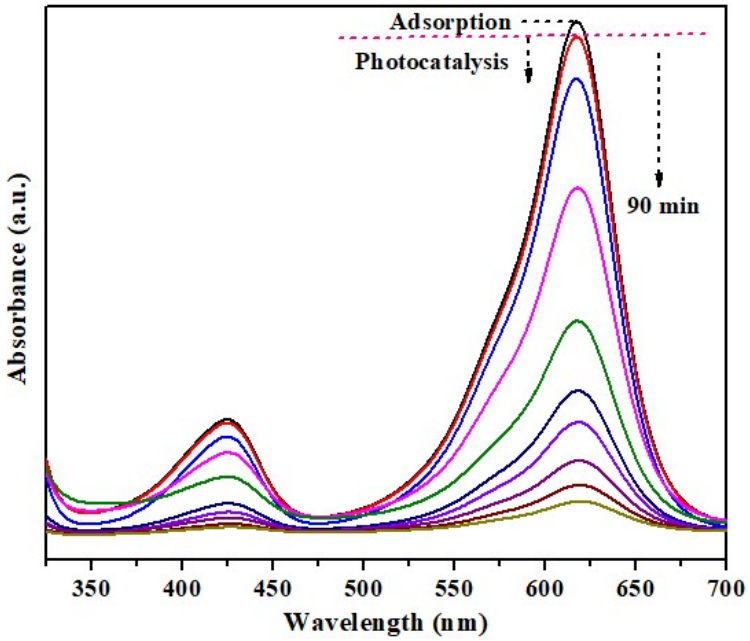

Fig. 8 Photocatalytic degradation of MG dye in the presence of biogenic ZnO NPs under solar irradiation

For 150 minutes in exposure to sunlight, the MG dye solution was investigated to determine the amount of deterioration at various concentrations (10, 15, 20, and 25 mg/L). The findings verified (Fig.9) that there was indeed a considerable decrease in deficiency with an increase in the primary dye concentration. The starting concentration of 25 mg/L indicated the highest deterioration of 95.7% under exposure to sunlight. This occurs because a higher dye concentration causes the solution to absorb a greater amount of light, which leaves less light available for the photocatalytic procedure to take place [53]. Furthermore, the photocatalytic activity is mitigated at high initial concentration of dye, through lowering the path length of the photon moving into the solution [54]. As a result, the production of unstable radicals as well as charge carriers decreased simultaneously, which slowed down the photodegradation

activity [55]. The current study found that the deterioration efficacy of MG dye was higher at 25 mg/L concentration. Additionally, at this particular concentration, the effects of scavengers, pH and catalyst dose were also investigated.

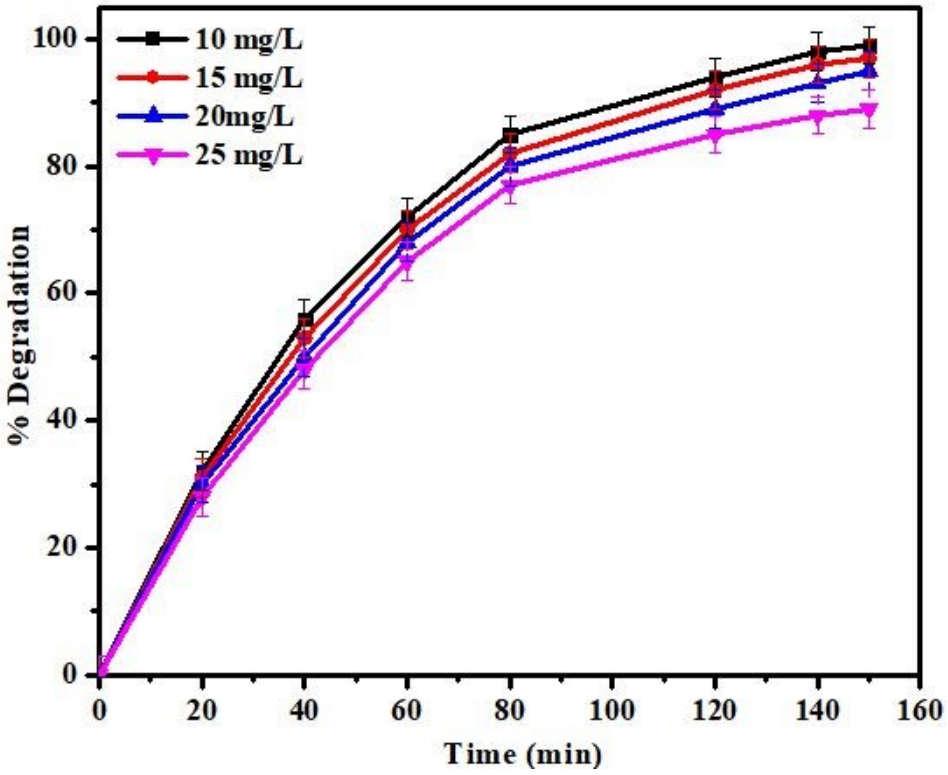

Fig. 9 Effect of MG dye concentration on the degradation efficiency

The photocatalytic activity gets better with the increase in the photocatalyst dosage. About 30.1%, 59.2%, 84.3%, 95.7 and 95.0% of MG dye was degraded with 10 mg (Z-I), 15 mg (Z-II), 20 mg (Z-III), 25 mg (Z-IV) and 30 mg (Z-V) of the ZnO photocatalyst in 150 min of light exposure (Fig. 10). The photocatalyst dosage of 25 mg results in the maximum deterioration the efficacy of 95.7%. It happens as a result of increased photocatalyst dosage, which generates more charge carriers that can engage in redox reactions when exposed to sunlight. Relatively lower degradation efficiency occurs at 30 mg of photocatalyst. In actuality, turbidity results from the addition of more photocatalyst and high concentrations may cause light screening, which reduces the catalyst's ability to absorb light [17].

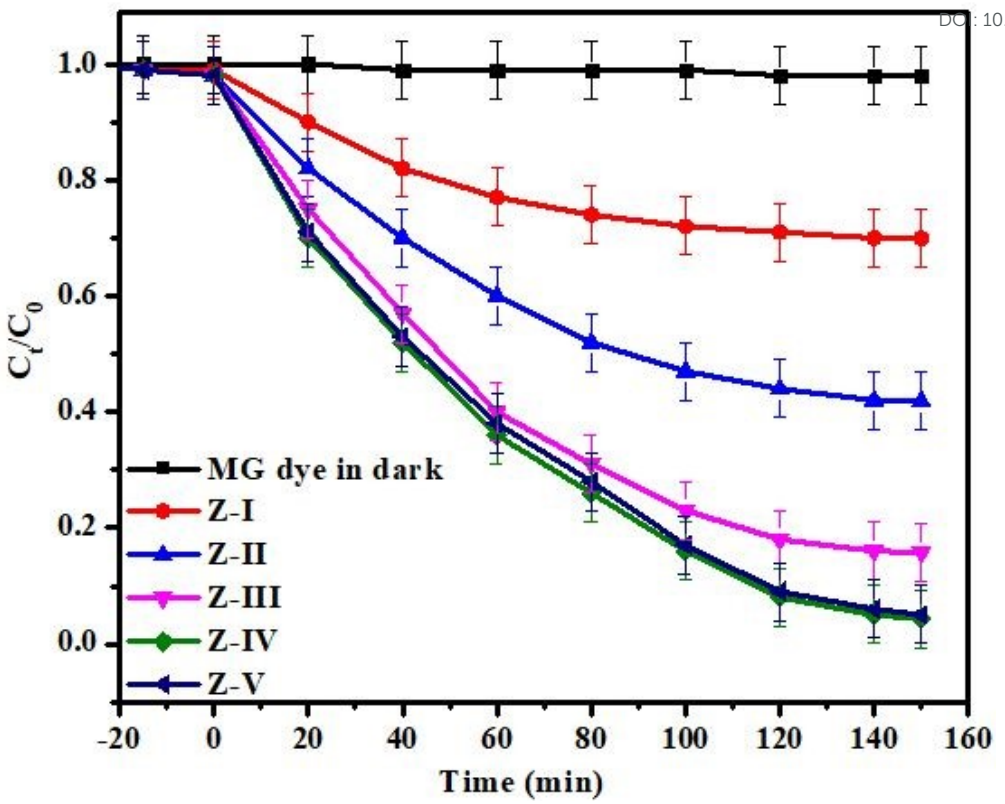

Fig. 10 Plots of the concentration of MG dye in aqueous solutions during specific time intervals with different amounts of ZnO NPs photocatalyst

For different dosages of the photocatalyst, the $\ln(C_t/C_0)$ vs. time plots are linear, suggesting that MG dye degradation occurs with pseudo-first order reaction kinetics (Fig. 11). The graph's slope is used to calculate the photocatalytic decomposition reaction's rate constant (k). The rate constants (k) for Z-I, Z-II, Z-III, Z-IV and Z-V were found to be in order, 0.00218, 0.00572, 0.01284, 0.0215 and 0.02037 min^{-1}. Based on the collected data, the rate constant (k) rose as the dosage of photocatalyst increased.

View Article Online
DOI: 10.1039/D5NJ02044A

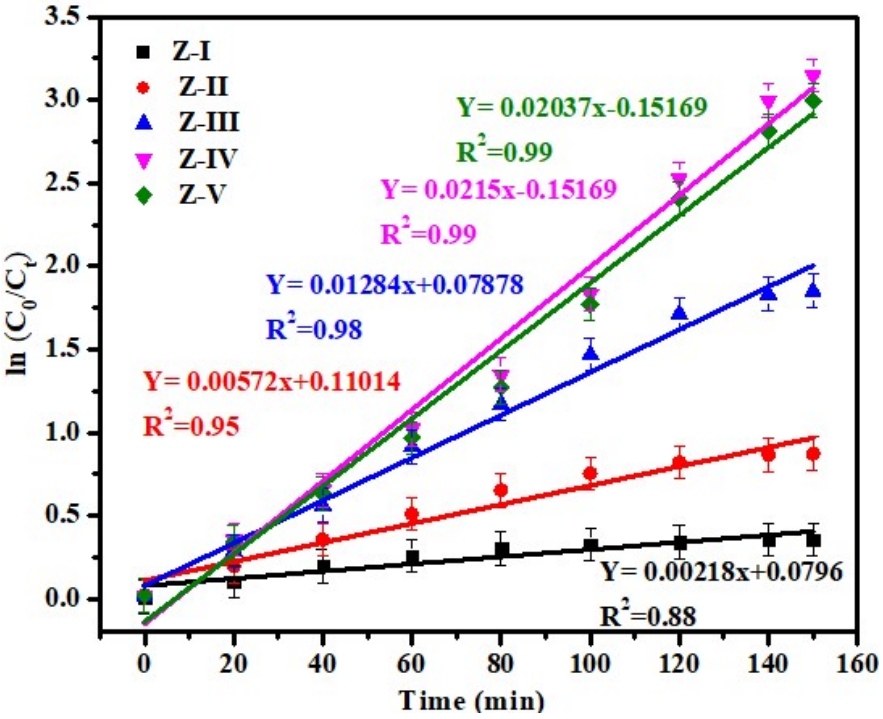

Fig. 11 Graph of $\ln(C_0/C_t)$ against time for ZnO NPs photocatalysts

Probably the greatest significant factor influencing the surface area of the catalyst and the features dye solution is pH. The molecular structure, colour, and composition are all greatly influenced by the pH of the solution. At pH values from 3 to 10, the impact of pH on the ZnO NPs photodegradation performance was examined (Fig. 12). The photodegradation improves when the pH rises from acidic to neutral, as the results show. Degradation was extreme in a neutral environment. The deterioration of the MG occurred in pH≤ 7 because of the existence of OH radicals. As a result, the observed value decreased, but the dye did not deteriorate. On the other hand, MG dye did not degrade appreciably at lower pH because of the interaction of ·OH radicals with positively charged ions.

View Article Online
DOI: 10.1039/D5NJ02044A

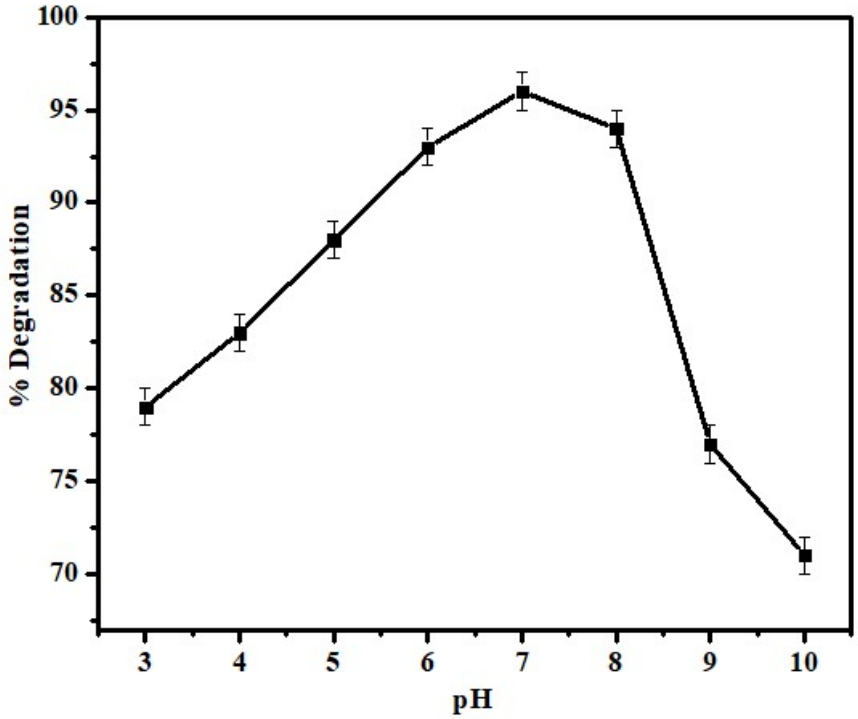

Fig. 12 Influence of pH on the degradation of MG dye over ZnO NPs photocatalyst

3.3.1 Intermediates in the MG dye photocatalytic pathway

Malachite green (MG) molecules were analysed using high-resolution mass spectrometry (HRMS) to determine the intermediates formed during degradation, thereby gaining a better understanding of the process (Fig. S3). The molecular mass of the MG cationic dye without chlorine is shown by the mass peak that the MG dye exhibits at m/z 329. The MG peak at m/z 329 vanished within 5 minutes of the catalyst being added, and other additional peaks that represented degradation intermediates or by-products developed (Fig. 13). The examination of these intermediates revealed two different degradation pathways: (a) MG's N-demethylation produced intermediates 1a (m/z 315), 1b (m/z 301), and 1c (m/z 273). After the chromophore underwent oxidative cleavage and deamination, the intermediate 1c yielded 1d (m/z 195), which in turn produced mineralization products. (b) In a different route, the chromophore of MG was oxidatively cleaved by radicals to produce 4-(dimethyl amino) phenol (3a, m/z 137) and Michler's ketone (2a). Following N-demethylation, the intermediate 2a yielded 2b (m/z 226), which likewise formed mineralized products following a number of oxidative breakdown stages.

View Article Online
DOI: 10.1039/D5NJ02044A

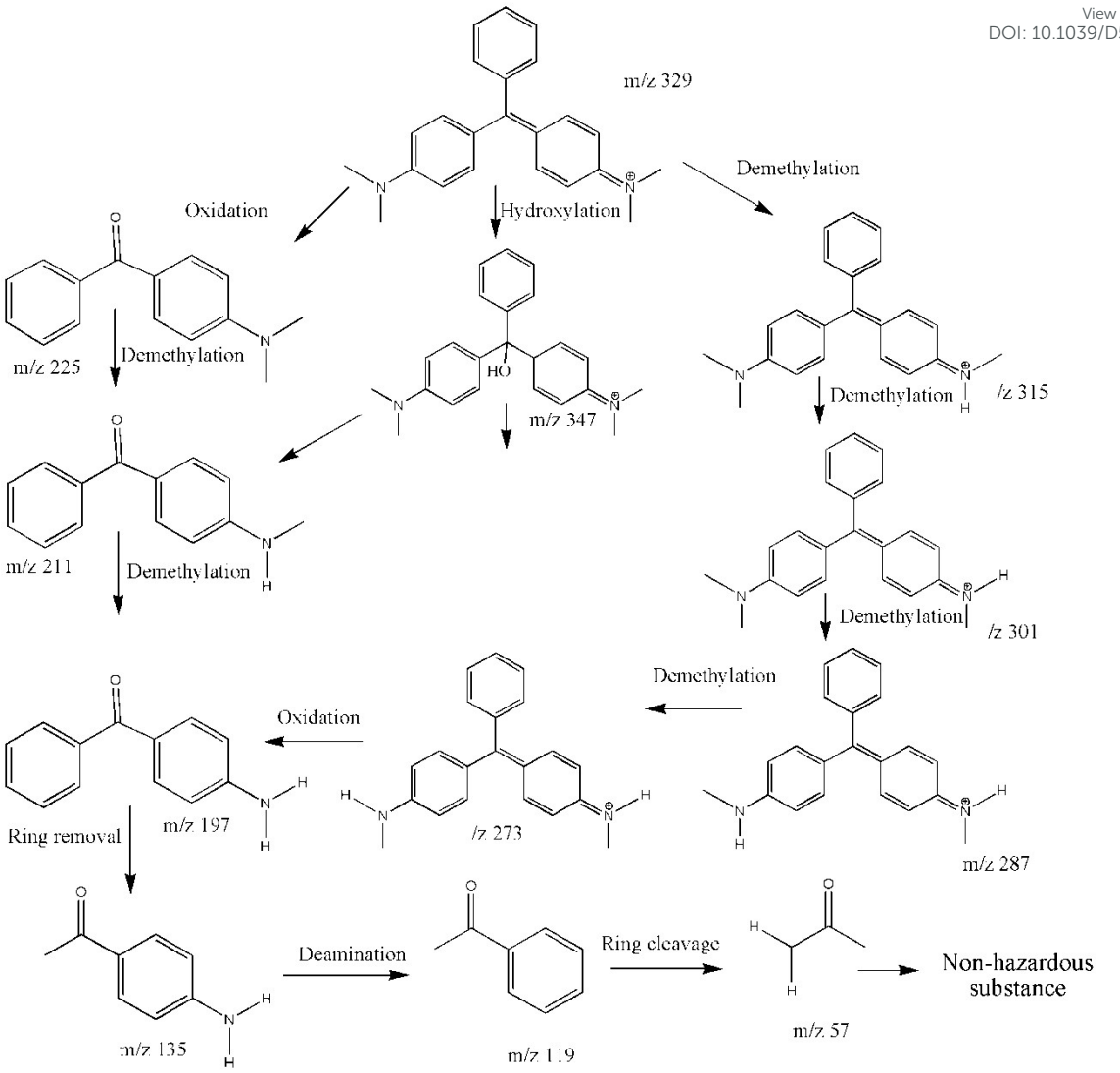

Fig. 13 Intermediate generation during MG dye photocatalysis over ZnO NPs photocatalyst

3.3.2 Recyclability and stability of biogenic ZnO nanoparticles

To examine the recyclability of the as-prepared ZnO photocatalyst, throughout this investigation, four successive cycles of solar light irradiation were conducted using the same experimental setup. The as-synthesized catalyst was extracted from every run using centrifugation to ensure it could be utilized in the subsequent run. The potential of ZnO photocatalyst to degrade the MG dye was reduced from 95.7% for the first run to 87.2% after the fourth consecutive run. It demonstrated the material's outstanding stability and potential for recycling. The reason for the slight decline in activity following the fourth run was the catalyst's unavoidable diffusion throughout the reclamation process, as well as the dye's and its breakdown byproducts' blocking of surface-active sites.

Fig. 14 shows the biogenic ZnO photocatalyst's XRD patterns both before and following its employment in four photocatalytic testing runs. The recycled sample's XRD pattern reveals no appreciable alterations, indicating that the photocatalyst's crystallinity was successfully preserved even after four photocatalytic studies' usage and that it remained remarkably stable under additional experimental conditions and solar radiation.

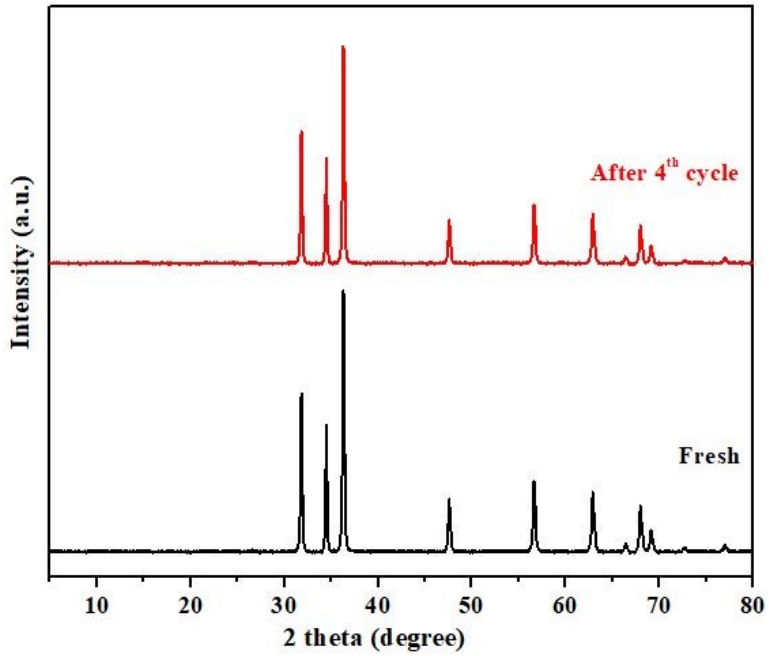

Fig. 14 XRD pattern of fresh and recycled ZnO NPs photocatalyst

Zinc oxide nanoparticles (ZnO-NPs) are widely celebrated in photocatalysis for their low cost, non-toxicity, thermal stability, and high electron mobility (100–300 $cm^2 V^{-1} s^{-1}$), making them effective in generating reactive oxygen species for pollutant degradation. Compared to TiO_2, ZnO offers broader UV absorption and stronger oxidative potential due to its direct band gap (~3.37 eV) [56]. However, despite these advantages, ZnO-NPs face several drawbacks. Notably, the bio-capping agents from *S. crassa* may mitigate aggregation and enhance UV-visible response, suggesting a promising route toward a more robust and efficient green photocatalyst.

The photocatalytic, antioxidant, and antidiabetic properties of the as-prepared ZnO NPs were determined and compared to several previously reported algal species-based ZnO NPs (Table S2), demonstrating the amazing capabilities of the current study.

4. Conclusion

This study demonstrated the bio-fabrication of highly efficient and environmentally friendly ZnO NPs facilitated by the cell-free extract of the well-known *S. crassa* algal species. Using FTIR, XRD, HRTEM, BET, XPS, FESEM and EDS techniques, the synthesised ZnO nanoparticles were characterised. The biosynthesized ZnO NPs from *S. crassa* have shown significant potential for the degradation of MG dye. These bio-fabricated ZnO NPs showed incredible adsorption capacity and attained a removal efficacy for MG dye. The biogenic ZnO NPs efficiently degraded 95.7% of MG dye within 150 minutes under the irradiation of direct sunlight. These results confirmed that bio-fabricated ZnO NPs have potential for wastewater treatment. This advantage is likely ascribed to the extensive spectrum of sunlight, which proficiently stimulates electrons in ZnO NPs, producing abundant reactive oxygen species (ROS) for MG dye degradation. Additionally, the biogenic ZnO NPs demonstrated significant antidiabetic potential as the sample displayed the highest percentage of enzyme inhibition (74.25 % ± 2.7) at 30 µg/mL concentration, with IC50 values for α-amylase and α-glucosidase at 18.69 µg/mL and 19.06 µg/mL, respectively. In the antioxidant test, the highest percentage of 2,2-diphenyl-1-picrylhydrazyl hydrate (DPPH) scavenging activity was 85.15 % ± 3.2, with an IC50 value of 17.90 µg/mL. The study suggests a sustainable and eco-friendly method for the treatment of wastewater. The biosynthesized ZnO NPs from *S. crassa* demonstrate excellent adsorption and photocatalytic capabilities, making them an auspicious solution for numerous environmental remediation challenges.

References

1. Kaur H, Kumar S, Kaushal S, Badru R, Singh PP, Pugazhendhi A. Highly customized porous TiO_2-PANI nanoparticles with excellent photocatalytic efficiency for dye degradation. Environ Res. 2023;225:114960. https://doi.org/10.1016/j.envres.2022.114960.
2. Kaushal S, Kumari V, Singh PP. Sunlight-driven photocatalytic degradation of ciprofloxacin and organic dyes by biosynthesized rGO-ZrO_2 nanocomposites. Environ Sci Pollut Res Int. 2023;30:65602-65617. doi:10.1007/s11356-023-27000-6.
3. Jalandhara D, Kumar S, Dalal J, Supreet, Singh G, Kumar S, et al. A multifunctional Co-doped $BiFeO_3$ nanocomposite: a promising candidate for photocatalytic degradation, antibacterial activity, and antioxidant applications. Mater Adv. 2025;6:641-657. https://doi.org/10.1039/D4MA01053A.
4. Sharmila A, Darshan AR, Hadkar VM, Sishu NK, Selvaraj CI. Green fabrication of *Hildegardia populifolia* (Roxb.) derived MgO nanoparticles exhibiting potential

antioxidant, antibacterial, and photocatalytic properties. Inorg Chem Commun. 2025;172:113730. https://doi.org/10.1016/j.inoche.2024.113730.

5. Kumaran AV, Sharmila A, Hadkar VM, Sishu NK, Mohanty C, Roopan SM, et al. Sustainable production of ZnO/MgO nanocomposite for effective photocatalytic degradation of Rhodamine B and their other properties. Mater Sci Eng B. 2025;313:117866. https://doi.org/10.1016/j.mseb.2024.117866.
6. Sishu NK, Selvaraj CI. Biogenic Ag-CuO nanocomposite fabricated using *Cichorium intybus* L. root extract: A dual approach for biological investigations and photocatalytic degradation of norfloxacin. Surf Interfaces. 2025a;66:106569. https://doi.org/10.1016/j.surfin.2025.106569.
7. Nair A, Kumawat YK, Choudhary S, Nath J, Sharma K, Rasool T, et al. Malachite green dye adsorption from wastewater using pine gum-based hydrogel: Kinetic and thermodynamic studies. J Mol Struct. 2024;1295:136671. https://doi.org/10.1016/j.molstruc.2023.136671.
8. Katyal K, Kumar S, Gaur J, Kalia R, Alam MW, Kaur H, et al. Phyto-engineered zinc oxide nanoparticles with tunable morphology for sustainable environmental and biomedical applications. Inorg Chem Commun. 2025;179:114859. https://doi.org/10.1016/j.inoche.2025.114859.
9. Kaushal S, Badru R, Kumar S, Kaur H, Singh PP. Efficient removal of cationic and anionic dyes from their binary mixtures by organic–inorganic hybrid material. J Inorg Organomet Polym. 2018;28:968-977. https://doi.org/10.1007/s10904-018-0817-8.
10. Sharma AK, Priya, Kaith BS, Sharma N, Bhatia JK, Tanwar V, et al. Selective removal of cationic dyes using response surface methodology optimized gum acacia-sodium alginate blended superabsorbent. Int J Biol Macromol. 2019;124:331-345. https://doi.org/10.1016/j.ijbiomac.2018.11.213.
11. Mandvi, Singh PP, Ballal S, Chahar M, Bansal J, Kumar R, et al. Construction of a 3D flower-like NiO/Mn_3O_4 heterojunction using Tulsi leaf extract for enhanced photodegradation of thiamethoxam pesticide and organic dyes under direct sunlight. Mater Adv. 2024;5:8097-8110. https://doi.org/10.1039/D4MA00708E.
12. Peighambardoust SJ, Boffito DC, Foroutan R, Ramavandi B. Sono-photocatalytic activity of sea sediment@400/ZnO catalyst to remove cationic dyes from wastewater. J Mol Liq. 2022;367:120478. https://doi.org/10.1016/j.molliq.2022.120478.
13. Saber AI, Sharma K, Aggarwal S, Babbar A, Kumar R, Kaur A, et al. Efficient photocatalytic degradation of tetracycline antibiotic and malachite green dye using La-

BDC MOFs. Emerg Mater. 2024;7:1019-1030. https://doi.org/10.1007/s42247-024-00644-x.

14. Bano K, Singh PP, Saeed SM, Aggarwal S, Kumar R, Kaushal S. Construction of honey bee hive-like CuO/PbO heterojunction photocatalysts with enhanced antibiotic and dye degradation activity under visible light. Environ Sci Water Res Technol. 2024;10:1714-1725. https://doi.org/10.1039/D4EW00270A.
15. Sartape AS, Mandhare AM, Jadhav VV, Raut PD, Anuse MA, Kolekar SS. Removal of malachite green dye from aqueous solution with adsorption technique using *Limonia acidissima* (wood apple) shell as low-cost adsorbent. Arab J Chem. 2017;10:S3229-S3238. doi: 10.1016/j.arabjc.2013.12.019.
16. Chen Z, Liu Y, Wei W, Ni BJ. Recent advances in electrocatalysts for halogenated organic pollutant degradation. Environ Sci Nano. 2019;6:2332-2366. https://doi.org/10.1039/C9EN00411D.
17. Kaushal S, Singh PP, Kaur N. Metal organic framework-derived Zr/Cu bimetallic photocatalyst for the degradation of tetracycline and organic dyes. Environ Nanotechnol Monit Manag. 2022;18:100727. https://doi.org/10.1016/j.enmm.2022.100727.
18. Singh S, Kaushal S, Kaur J, Kaur G, Mittal SK, Singh PP. CaFu MOF as an efficient adsorbent for simultaneous removal of imidacloprid pesticide and cadmium ions from wastewater. Chemosphere. 2021;272:129648. https://doi.org/10.1016/j.chemosphere.2021.129648.
19. Kaushal S, Kumar A, Bains H, Singh PP. Photocatalytic degradation of tetracycline antibiotic and organic dyes using biogenic synthesized CuO/Fe_2O_3 nanocomposite: pathways and mechanism insights. Environ Sci Pollut Res. 2023;30:37092-37104. https://doi.org/10.1007/s11356-022-24848-y.
20. Kumari V, Kaushal S, Singh PP. Green synthesis of a CuO/rGO nanocomposite using a *Terminalia arjuna* bark extract and its catalytic activity for the purification of water. Mater Adv. 2022;3:2170-2184. https://doi.org/10.1039/D1MA00993A.
21. Sishu NK, Selvaraj CI. Bio-fabrication of *Cichorium intybus* L. root aqueous extract mediated ZnO nanoparticle (CIRAE-ZnO NP) for its promising therapeutic applications. Green Chem Lett Rev. 2025b;18(1). DOI:10.1080/17518253.2025.2489461.
22. Fang J, Xu X, Yang Y, Han Z, Zuo Z, Han W, et al. An integrated $ZnO–SnO_2$ n–n heterostructure strategy of catalysts and ash for promoting diesel soot combustion. J Therm Anal Calorim. 2025. https://doi.org/10.1007/s10973-025-14184-x.

23. Jha S, Rani R, Singh S. Biogenic Zinc Oxide nanoparticles and their biomedical applications: a review. J Inorg Organomet Polym. 2023;33:1437-1452. https://doi.org/10.1007/s10904-023-02550-x.
24. Ravi P, Babu S. Recent development in plant-mediated zinc oxide nanoparticles with biomedical applications. Chem Phys. 2025;10:100870. https://doi.org/10.1016/j.chphi.2025.100870.
25. Chandrasekaran S, Anbazhagan V, Anusuya S. Green route synthesis of ZnO nanoparticles using *Senna auriculata* aqueous flower extract as reducing agent and evaluation of its antimicrobial, antidiabetic and cytotoxic activity. Appl Biochem Biotechnol. 2023;195:3840-3854. https://doi.org/10.1007/s12010-022-03900-0.
26. Maheo AR, Vithiya BS, Prasad TA, Mangesh VL, Perumal T, Al-Qahtani WH, et al. Cytotoxic, antidiabetic, and antioxidant study of biogenically improvised *Elsholtzia blanda* and chitosan-assisted zinc oxide nanoparticles. ACS Omega. 2023;8:10954-10967. https://doi.org/10.1021/acsomega.2c07530.
27. Sodhi RS, Singh PP, Lal B, Joshi SK, Kumar R, Singh Y, et al. Biogenic synthesis of ZnO nanoparticles using *Polystichum squarrosum* extract and its applications as anti-oxidant, anti-diabetic agent, and industrial wastewater treatment. Emerg Mater. 2023;7:285-298. http://dx.doi.org/10.1007/s42247-023-00589-7.
28. Sharma K, Kaushal S, Jain A, Sami MH, Kumar S, Tariq H, et al. A comprehensive review on biogenic synthesis of bimetallic nanoparticles and their application as catalytic reduction of 4-nitrophenol. Chem Pap. 2024;78:2757-2782. https://doi.org/10.1007/s11696-024-03323-7.
29. Kaur R, Kaushal S, Singh PP. Biogenic synthesis of a silver nanoparticle–SnZrMoP nanocomposite and its application for the disinfection and detoxification of water. Mater Adv. 2020;1:728-737. https://doi.org/10.1039/D0MA00096E.
30. Song G, Zeng C, Li J, Liu J, Zhao J, Liu B, et al. Exosome-based nanomedicines for digestive system tumors therapy. Nanomedicine (Lond). 2025;20:1167-1180. doi:10.1080/17435889.2025.2493037.
31. Jacob JM, Ravindran R, Narayanan M, Samuel SM, Pugazhendhi A, Kumar G. Microalgae: A prospective low-cost green alternative for nanoparticle synthesis. Curr Opin Environ Sci Health. 2021;20:100163. https://doi.org/10.1016/j.coesh.2019.12.005
32. Singh Y, Sodhi RS, Singh PP, Kaushal S. Biosynthesis of NiO nanoparticles using *Spirogyra* sp. cell-free extract and their potential biological applications. Mater Adv. 2022;3:4991-5000. https://doi.org/10.1039/D2MA00114D

33. Zhang YW, Zheng XW, Liu YJ, Fang L, Pan ZF, Bao MH, et al. Effect of Oridonin on Cytochrome P450 Expression and Activities in HepaRG Cell. Pharmacology. 2018;101:246–254. doi:10.1159/000486600
34. Kumar V, Singh Y, Kaushal S, Kumar R. Bioinspired synthesis of copper oxide nanoparticles using aqueous extracts of *Cladophora glomerata* and their potential biomedical applications. Bioprocess Biosyst Eng. 2025;10:1-13. doi:10.1007/s00449-025-03133-5
35. Uzai B, Liaqat A, Iqbal H, Menaa B, Razzaq A, Thiripuranathar G, et al. Green and cost-effective synthesis of metallic nanoparticles by algae: safe methods for translational medicine. Bioengineering. 2020;7:129. doi:10.3390/bioengineering7040129
36. Zhu Q, Sun J, An C, Li X, Xu S, He Y, et al. Mechanism of LncRNA Gm2044 in germ cell development. Front Cell Dev Biol. 2024;12:1410914. doi:10.3389/fcell.2024.1410914
37. Abdel-Aal EI, Haroon AM, Mofeed J. Successive solvent extraction and GC–MS analysis for the evaluation of the phytochemical constituents of the filamentous green alga *Spirogyra longata*. Egypt J Aquat Res. 2015;41:233-246. https://doi.org/10.1016/j.ejar.2015.06.001
38. Hameed H, Waheed A, Sharif MS, Saleem M, Afreen A, Tariq M, et al. Green synthesis of Zinc Oxide (ZnO) nanoparticles from green algae and their assessment in various biological applications. Micromachines. 2023;14:928. https://doi.org/10.3390/mi14050928
39. Sharif MS, Hameed H, Waheed A, Tariq M, Afreen A, Kamal A, et al. Biofabrication of Fe_3O_4 nanoparticles from *Spirogyra hyalina* and *Ajuga bracteosa* and their antibacterial applications. Molecules. 2023;28:3403. doi:10.3390/molecules28083403
40. Lisec J, Schauer N, Kopka J, Willmitzer L, Fernie AR. Gas chromatography mass spectrometry–based metabolite profiling in plants. Nat Protoc. 2006;1:387-396. https://doi.org/10.1038/nprot.2006.59
41. Devi VA, Kalaiselvi V. Nanoparticles reactions in cervical cancer: challenge and hope. J Nanosci Nanotechnol. 2022;7:12. doi:10.12769/IPNNR.23.7.022
42. Mandal AK, Katuwal S, Tettey F, Gupta A, Bhattarai S, Jaisi S, et al. Current research on zinc oxide nanoparticles: synthesis, characterization, and biomedical applications. Nanomaterials. 2022;12:3066. https://doi.org/10.3390/nano12173066
43. Sharma R, Kumar N, Sharma P, Yadav A, Aggarwal NK. Biosynthesis, characterisation and therapeutic potential of green coconut waste derived zinc oxide nanoparticles. Surf Interfaces. 2025;18:100372. https://doi.org/10.1016/j.rsurfi.2024.100372

44. Faisal S, Khan MA, Jan H, Shah SA, Abdullah A, Shah S, et al. Edible mushroom (*Flammulina velutipes*) as bio-source for silver nanoparticles: from synthesis to diverse biomedical and environmental applications. Nanotechnology. 2020;32:065101. https://doi.org/10.1088/1361-6528/abc2eb
45. Manikandan R, Anand AV, Kumar S, Pushpa P. Phytochemical and in vitro antidiabetic activity of *Psidium guajava* leaves. Pharmacogn J. 2016;8:392-394.
46. Majeed S, Danish M, Zakariya NA, Hashim RR, Ansari MT, Alkahtani S, et al. In vitro evaluation of antibacterial, antioxidant, and antidiabetic activities and glucose uptake through 2-NBDG by Hep-2 liver cancer cells treated with green synthesized silver nanoparticle. Oxid Med Cell Longev. 2022;1-14. https://doi.org/10.1155/2022/1646687
47. Saber AI, Sharma K, Aggarwal S, Babbar A, Kumar R, Kaur A, et al. Efficient photocatalytic degradation of tetracycline antibiotic and malachite green dye using La-BDC MOFs. Emergent Mater. 2024;7:1019-1030. https://doi.org/10.1007/s42247-024-00644-x
48. Xiao X, Peng B, Cai L, Zhang X, Liu S, Wang Y. The high efficient catalytic properties for thermal decomposition of ammonium perchlorate using mesoporous $ZnCo_2O_4$ rods synthesized by oxalate co-precipitation method. Sci Rep. 2018;8:7571. doi:10.1038/s41598-018-26022-2
49. Pawar RC, Lee CS. Single-step sensitization of reduced graphene oxide sheets and CdS nanoparticles on ZnO nanorods as visible-light photocatalysts. Appl Catal B. 2014;144:57-65. doi:10.1016/j.apcatb.2013.06.022
50. Kim YH, Heo JS, Kim TH, Park S, Yoon MH, Kim J, et al. Flexible metal-oxide devices made by room-temperature photochemical activation of sol–gel films. Nature. 2012;489:128-132. doi:10.1038/nature11434
51. Supin KK, Namboothiri PM, Vasundhara M. Enhanced photocatalytic activity in ZnO nanoparticles developed using novel *Lepidagathis ananthapuramensis* leaf extract. RSC Adv. 2023;13:1497-1515. https://doi.org/10.1039/D2RA06967A
52. Rambabu K, Bharath G, Banat F, Show PL. Green synthesis of zinc oxide nanoparticles using *Phoenix dactylifera* waste as bioreductant for effective dye degradation and antibacterial performance in wastewater treatment. J Hazard Mater. 2020;15:123560. doi:10.1016/j.jhazmat.2020.123560
53. Reza KM, Kurny A, Gulshan F. Parameters affecting the photocatalytic degradation of dyes using TiO_2: a review. Appl Water Sci. 2015;7:1569-1578. doi:10.1007/s13201-015-0367-y

54. Saggioro EM, Oliveira AS, Pavesi T, Maia CG, Ferreira LFV, Moreira JC. Use of titanium dioxide photocatalysis on the remediation of model textile wastewaters containing azo dyes. Molecules. 2011;16:10370-10386. doi:10.3390/molecules161210370

55. Chen T, Cao C, Chen T, Ding X, Huang H, Shen L, et al. Unravelling highly tunable selectivity in CO_2 hydrogenation over bimetallic In-Zr oxide catalysts. ACS Catal. 2019;9:8785-8797. doi:10.1021/acscatal.9b01869

56. Zhu C, Wang X. Nanomaterial ZnO synthesis and its photocatalytic applications: a review. Nanomaterials. 2025;15:82. https://doi.org/10.3390/nano15090682

Data availability statement

The data that support the findings of this study are available from Royal Society of Chemistry, but restrictions apply to the availability of these data, which were used under license for the current study, and so are not publicly available. Data are however available from the authors upon reasonable request and with permission of Royal Society of Chemistry.